INTERFACE

royalsocietypublishing.org/journal/rsif

Research

Cite this article: Treado JD, Roddy AB, Théroux-Rancourt G, Zhang L, Ambrose C, Brodersen CR, Shattuck MD, O'Hern CS. 2022 Localized growth and remodelling drives spongy mesophyll morphogenesis. *J. R. Soc. Interface* **19**: 20220602. https://doi.org/10.1098/rsif.2022.0602

Received: 18 August 2022
Accepted: 14 November 2022

Subject Category:
Life Sciences–Physics interface

Subject Areas:
biophysics, biomechanics

Keywords:
mathematical modelling of development, leaf spongy mesophyll, self-assembly

Author for correspondence:
John D. Treado
e-mail: john.treado@yale.edu

†Present address: Max Planck Institute for the Physics of Complex Systems, Dresden, Germany.

Electronic supplementary material is available online at https://doi.org/10.6084/m9.figshare.c.6307516.

THE ROYAL SOCIETY PUBLISHING

Localized growth and remodelling drives spongy mesophyll morphogenesis

John D. Treado[1,†], Adam B. Roddy[5], Guillaume Théroux-Rancourt[6], Liyong Zhang[7], Chris Ambrose[7], Craig R. Brodersen[2], Mark D. Shattuck[8] and Corey S. O'Hern[3,4]

[1]Department of Mechanical Engineering and Materials Science and Integrated Graduate Program in Physical and Engineering Biology, [2]School of the Environment, [3]Department of Physics, and [4]Department of Applied Physics, Yale University, New Haven, CT 06520, USA
[5]Institute of Environment, Department of Biological Sciences, Florida International University, Miami, FL 33199, USA
[6]University of Natural Resources and Life Sciences, Vienna, Department of Integrative Biology and Biodiversity Research, Institute of Botany, 1180 Vienna, Austria
[7]Department of Biology, College of Arts and Science, University of Saskatchewan, Saskatoon, Canada S7N 5E2
[8]Department of Physics and Benjamin Levich Institute, City College of New York, NY 10031, USA

JDT, 0000-0002-2053-4566; GT-R, 0000-0002-2591-0524; CRB, 0000-0002-0924-2570

The spongy mesophyll is a complex, porous tissue found in plant leaves that enables carbon capture and provides mechanical stability. Unlike many other biological tissues, which remain confluent throughout development, the spongy mesophyll must develop from an initially confluent tissue into a tortuous network of cells with a large proportion of intercellular airspace. How the airspace in the spongy mesophyll develops while the tissue remains mechanically stable is unknown. Here, we use computer simulations of deformable polygons to develop a purely mechanical model for the development of the spongy mesophyll tissue. By stipulating that cell wall growth and remodelling occurs only near void space, our computational model is able to recapitulate spongy mesophyll development observed in *Arabidopsis thaliana* leaves. We find that robust generation of pore space in the spongy mesophyll requires a balance of cell growth, adhesion, stiffness and tissue pressure to ensure cell networks become porous yet maintain mechanical stability. The success of this mechanical model of morphogenesis suggests that simple physical principles can coordinate and drive the development of complex plant tissues like the spongy mesophyll.

1. Introduction

Morphogenesis, or the emergence of structure during biological development, requires the careful coordination of cell growth and motility across entire tissues. Plant tissues, in particular, require significant coordination because plant cells are not motile [1]. During development, plant cells undergo dramatic changes in their size, shape and number of neighbours [2–7]. For example, leaf epidermal pavement cells expand by several orders of magnitude and take on a diversity of shapes, depending on global factors such as organ growth anisotropy and local factors such as the mechanical stresses imposed by their immediate neighbours [5,8–10]. While there have been significant advances in characterizing and modelling tissue morphogenesis in plants, these efforts have been focused almost entirely on tissues composed of confluent cells [11,12]. However, mesophyll, an important tissue inside leaves where the photosynthesis occurs, is a porous assembly of both cells and intercellular air space. After entering the leaf through the stomata on the leaf surface, CO_2 must diffuse through the airspace and into the cells where it is converted into sugar [13,14]. While the upper layer of mesophyll, the palisade mesophyll, is composed of densely packed, elongated cells with the same orientation, the lower, spongy mesophyll is highly porous and composed of cells with many different shapes and orientations [15–17], leading to variation in

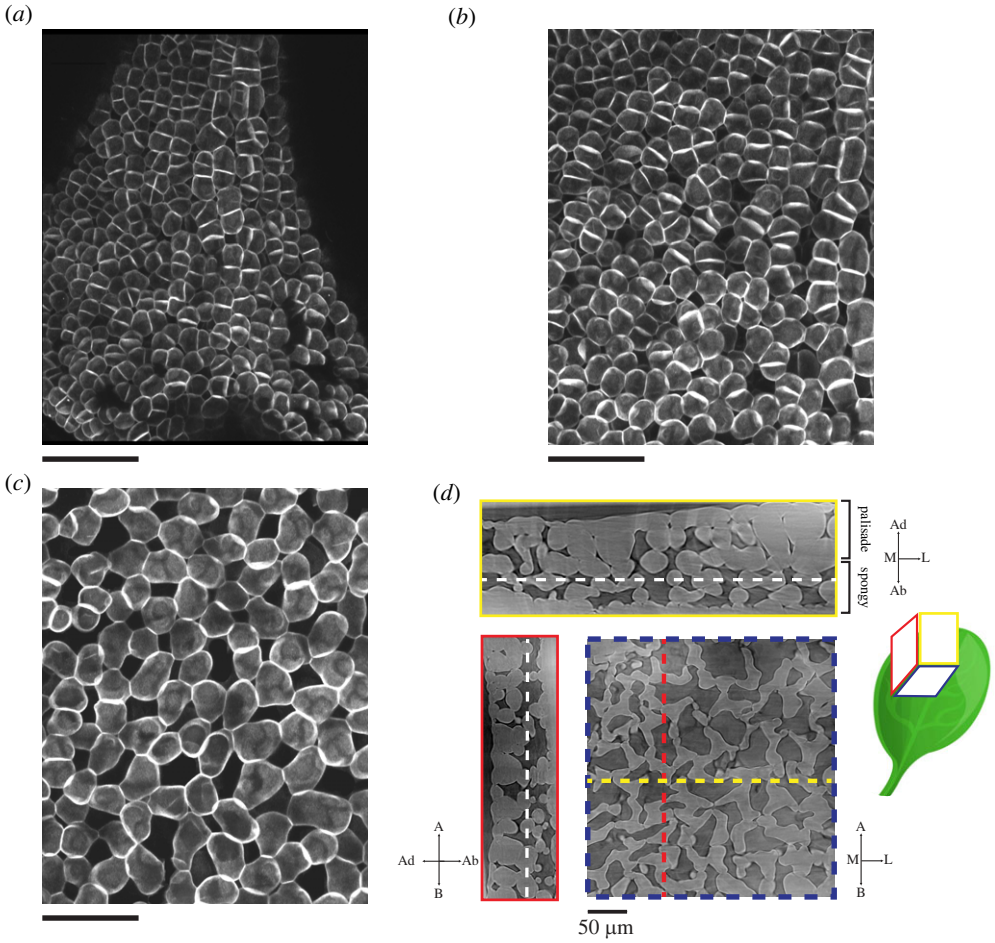

Figure 1. Confocal microscopic images of the developing spongy mesophyll in *Arabidopsis thaliana* taken at (*a*) 0, (*b*) 24 and (*c*) 72 hours of development. (See methods for details.) The black scale bar in each frame represents 50 µm. (*d*) Mesophyll tissue observed in a microcomputed tomography (microCT) scan of a mature *Arabdidopsis* leaf. The leaf has three orthogonal axes, the basal–apical (BA), medial–lateral (ML) and adaxial–abaxial (AdAb) axes. Leaf images are in the three planes orthogonal to these axes, i.e. the transverse (yellow), longitudinal (red) and paradermal (purple) planes, respectively. The paradermal slice is taken at the location of the dashed white lines drawn on the other slices, and the location of the transverse (longitudinal) slices are indicated by yellow (red) dashed lines on the paradermal slice.

carbon assimilation [18–20]. Yet, the spongy mesophyll cells begin development densely packed with nearly spherical cell shapes [21–23]. The cell mechanics and cell–cell interactions that control the formation of pore space in the spongy mesophyll are currently unknown [24].

Recent experimental advances in three-dimensional imaging have shed light on the development of complex cell shapes in both young and mature leaves [23,25,26]. Early in development, spongy mesophyll tissue is densely packed with each cell taking on a convex, polygonal shape in paradermal cross-section (figure 1). However, as the tissue grows, airspace begins to form between cells, and the tissue transitions from nearly confluent to porous. At maturity, cells in the spongy mesophyll form tortuous, quasi-two-dimensional (quasi-2D) porous networks [14,16,27]. The pore space forms due to cell expansion and the breaking of cell–cell contacts, not programmed cell death [21]. While cell adhesion [28], tissue pressure [29] and cell shape change [8,23,30] are known to be important for morphogenesis of the plant epidermis, it is unclear if or how they contribute to development of the spongy mesophyll. Computational modelling of tissue morphogenesis can provide answers to these open questions, and to our knowledge, no model has ever been developed for plant tissues that can vary in porosity along a developmental trajectory.

Here, we (i) develop computer simulations of deformable polygons with shape degrees of freedom [31,32] in two dimensions to recapitulate the developmental trajectory of the spongy mesophyll, (ii) compare these simulations with empirical images of spongy mesophyll development in the model plant species *Arabidopsis thaliana* (L.) Heynh, and (iii) test the sensitivity of our developmental model to variation in cell growth, cell–cell adhesion, cell mechanics and bulk tissue pressure. This approach reveals three key features that are necessary to capture the development of the spongy mesophyll microstructure observed in *A. thaliana* leaves [23]. First, while cell areal growth is constant throughout the tissue and during development, growth and remodelling of cell wall must be localized to cell boundaries *not* in contact with other cells, i.e. exposed to the intercellular airspace. Second, cells must balance cell wall bending rigidity with cell–cell adhesive strength to develop networks with evenly spaced pores. If cell walls are too stiff, or if adhesion is too weak and contacts break too frequently, then the networks can collapse. Third, the pressure inside the simulation boundary must be constant throughout the developmental trajectory. While cells expand during development due to positive turgor pressure [33], remodelling of cell wall near voids leads to localized growth that can cooperatively push the tissue boundary outwards. That is, the change in

the simulation domain size is not an independent variable in our simulations but instead arises from differences in the growth rates of cell perimeter and cell area. This computational model therefore demonstrates that a porous tissue as complex as the spongy mesophyll can be assembled by a simple set of mechanical rules.

2. Results

2.1. Adhesive, growing deformable polygons at constant pressure generate porous cell networks

To model the development of the spongy mesophyll in two spatial dimensions, we employ numerical simulations of deformable polygons (the DP model, see [31,32]) that can change the shape in response to stress as well as interact with each other via repulsive and attractive forces. While mesophyll morphogenesis is of course a three-dimensional process, pore-space development in *Arabidopsis* spongy mesophyll predominantly occurs in the paradermal plane [23], and nearly planar cell arrangement has been observed in a large number of other species [16]. Although extensions to three-dimensional modelling are necessary to understand tissue interfaces (i.e. between the spongy mesophyll and the epidermis), a two-dimensional approach is sufficient for understanding the pore-space structure within the spongy mesophyll.

Our simulations contain a collection of N polygons, each with n vertices. The dynamics of the polygons, which we will refer to as cells, are governed by forces due to changes in cell shape and forces due to cell–cell interactions. The potential energy $U_{\mu,\text{shape}}$ for changes in cell shape for cell μ is defined as folows:

$$U_{\mu,\text{shape}} = \frac{\epsilon_a}{2}\left(\frac{a_\mu}{a_{0\mu}} - 1\right)^2 + \sum_{i=1}^{n_\mu}\left[\frac{\epsilon_l}{2}\left(\frac{l_{i\mu}}{l_{0i\mu}} - 1\right)^2 + \frac{\epsilon_b}{2}(\theta_{i\mu} - \theta_{0i\mu})^2\right], \tag{2.1}$$

where ϵ_a, ϵ_l and ϵ_b are energy scales that control the amount of energy required to have cell areas a, perimeter segment lengths l and local curvatures θ that deviate from their preferred values (a_0, l_0 and θ_0, respectively). Each segment length is labelled l_μ and bending angle θ_μ, where $i = 1, \ldots, n_\mu$. A graphical representation of these quantities, as well as derivations of the forces due to each term in equation (2.1), are provided in electronic supplementary material, section S1. In these simulations, energies and lengths are measured in units of ϵ_a and the averaged square root of the cell area, i.e. $\rho = N^{-1}\sum_\mu \sqrt{a_{0\mu}}$. All vertices have unit mass, and time is measured in units of $\rho\epsilon_a^{-1/2}$.

The total potential energy U is the shape potential energy plus the potential energy contribution from cell–cell interactions,

$$U = \sum_{\mu=1}^{N}\left[U_{\mu,\text{shape}} + \sum_{\nu>\mu}\sum_{i=1}^{n_\mu}\sum_{j=1}^{n_\nu}\frac{\epsilon_{ij\mu\nu}}{2}\left(1 - \frac{r_{ij\mu\nu}}{\sigma_{ij\mu\nu}}\right)^2\right]. \tag{2.2}$$

Each vertex i on cell μ is a soft disc with diameter σ_μ, and $\epsilon_{ij\mu\nu}$ is an energy scale that controls the distance $r_{ij\mu\nu}$ to vertex j on cell μ. $\sigma_{ij\mu\nu} = (\sigma_\mu + \sigma_{j\nu})/2$ is the distance at which vertex i is in contact with vertex j. Vertices overlap when $r_{ij\mu\nu} < \sigma_{ij\mu\nu}$, and in this case, we set $\epsilon_{ij\mu\nu} = \epsilon_c$ such that all vertices repel with equal energy.

Mesophyll cells adhere to their neighbours [28,34], so we model attractive interactions between cells using harmonic bonds between vertices. If two vertices i and j and cells μ and ν are bonded, and $r_{ij\mu\nu} > \sigma_{ij\mu\nu}$, we set $\epsilon_{ij\mu\nu} = \epsilon_c/z_{\mu\nu}$, where $z_{\mu\nu} = (z_\mu + z_\nu)/2$, and z_μ is the number of cells in contact with cell μ. Thus, we assume that bond stiffness is inversely proportional to the current number of other cells with which a given cell is in contact. Bonds are broken with probability $p_{\text{off}} = \min\,[1, \exp\,(-\beta\Delta U)]$, where $\Delta U = U_0 - U_c$, U_c is the energy stored in the bond, U_0 is a fixed bond-breaking energy and β is an inverse effective temperature governing bond sensitivity. For a bond held between cells μ and ν, we define $U_0 = \epsilon_c z_{\mu\nu}^{-1}(1 - r^*/\sigma)^2/2$, where σ is the mean vertex diameter and r^* is the maximum bond length. As described in electronic supplementary material, section S2 we set $\epsilon_{ij\mu\nu} \to 0$ for $r_{ij\mu\nu} > \sigma_{ij\mu\nu}$ once a bond is broken and do not reform bonds once they are broken.

Our simulations begin with densely packed cells that reflect the nearly confluent, nascent spongy mesophyll tissue, and they grow to form porous cell networks (figure 2*e*) [21–23,35]. To form a dense initial state, we isotropically compress dilute configurations of cells by small compression and potential energy minimization steps, similar to the previous work on model jammed materials [31,36], to a near-confluent state with less than 3% of the simulation domain occupied by void space. Once the initial near-confluent state is generated, adhesive bonds are formed between all overlapping vertices, and all spontaneous curvatures θ_0 at each vertex are set to their instantaneous θ values. This point defines the initial state with characteristics reflective of the earliest images of mesophyll development [21,37].

The full details of our model for plant cell growth and shape change are provided in electronic supplementary material, section S3 but are briefly summarized here. At the beginning of each simulation step, the *preferred* area a_0 of each cell is increased by an increment Δa, i.e.

$$a_0 \to a_0 + \Delta a. \tag{2.3}$$

We also change the *preferred* perimeter length segments l_0 each step by an increment Δl, i.e.

$$l_0 \to l_0 + \Delta l. \tag{2.4}$$

These perturbations to a_0 and l_0 induce an applied stress on the cell areas (i.e. pressure) and boundaries, which will eventually drive cell shape change and tissue growth. Because cell boundaries grow more quickly where they are adjacent to void space than where they are in contact with other cells [23], we apply a boundary stress only on the perimeter length segments (figure 2*b*, yellow arrows) whose vertices lack contacts with vertices of other DP cells (figure 2*b*, red disc). Δl depends on both a dimensionless scale parameter λ, which determines how fast the void-facing cell perimeter grows relative to the cell area, and c_L, which regulates how fast a given void segment grows compared with the other void segments (see table 1, and see further details in electronic supplementary material, section S3). We set $\Delta l = 0$ when the particle shape parameter exceeds a threshold $\mathcal{A}_{\max}$, which we set to 3, close to the maximum value of individual spongy mesophyll cells (approx. 2.9) [17,38].

In addition, the void-facing spontaneous curvature θ_0 is updated according to

$$\theta_0 \to \theta_0 - \Delta\theta, \tag{2.5}$$

where $\Delta\theta > 0$. Decreasing θ_0 near void drives cell shapes towards increasingly lobed structures, reminiscent of cell shapes in porous network configurations [15,16,21,35]

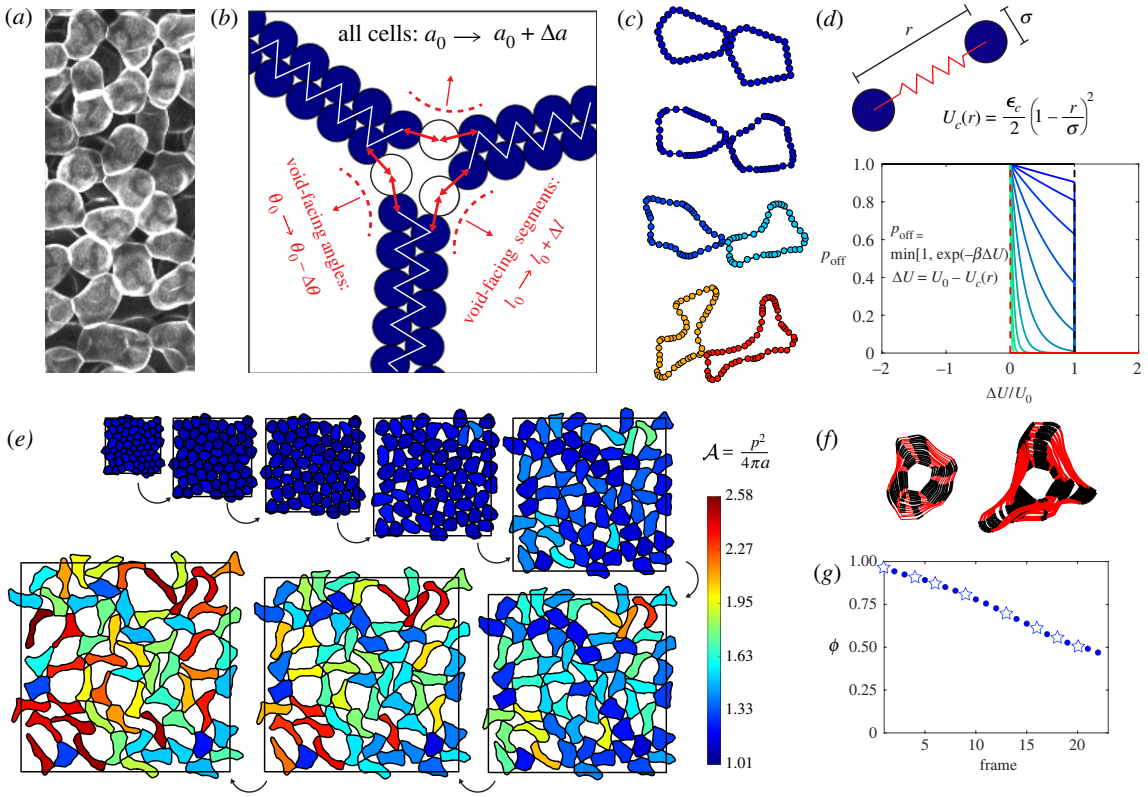

Figure 2. Summary of model for spongy mesophyll development in two dimensions. (*a*) Close-up of cell shape during spongy mesophyll development, taken from figure 1*c*. (*b*) Close-up of a tri-cellular junction using DP model cells, highlighting the model's growth rules: (i) all *preferred* areas change by $a_0 \rightarrow a_0 + \Delta a$, while (ii) preferred segment lengths and (iii) preferred bending angles change by $l_0 \rightarrow l_0 + \Delta l$ and $\theta_0 \rightarrow \theta_0 - \Delta\theta$ only near voids (white vertices). More details are given in §2.1 and electronic supplementary material, section S1. (*c*) DP model cells changing shape during the simulation of spongy mesophyll development, from top to bottom. Vertices of each DP model cell are drawn as discs with radius σ, as defined in (*d*). Disc colour is given by the DP cell shape parameter $\mathcal{A} = p^2/4\pi a$, and disc size is rescaled to be the same in each row. (*d*) A schematic of an inter-cellular bond between two vertices, as well as bond-breaking probability p_{off} as a function of the inverse effective temperature β (ranging from $\beta = 10$ to 500, colour sorted from blue to green). (See main text and electronic supplementary material section S2 for details.) (*e*) Sixty-four cells growing in periodic boundary conditions. Cells and the boundary are drawn to scale, and cell colour represents the cell shape parameter. (*f*) The boundaries of two cells from (*e*) drawn to scale. Black segments indicate vertices in contact with other cells, whereas red segments indicate vertices in contact with void. (*g*) Comparison of packing fraction ϕ between experiment and simulation in (*e*). Stars indicate specific frames from (*e*). The simulation in (*e*)–(*g*) used $\epsilon_b = 0.4$, $\beta = 100$ and $r^* = 2.4$. $\Delta a = 0.5$, $\lambda = 5$, $c_L = 0.5$, $c_B = 4$, $\theta_{0,\min} = -\pi/10$ and $P_0 = 10^{-3}$. See table 1 for parameter descriptions.

(dashed red lines in figure 2*b*). We set $\Delta\theta = 0$ when the preferred curvature becomes less than a target minimum value $\theta_{0,\min}$ (electronic supplementary material, section S3).

This model aims to recapitulate a vital feature of plant tissue development, that positive turgor pressure coupled with cell wall remodelling drives both plant cell growth and plant cell shape change [33]. We induce positive turgor pressure in each cell by growing a_0 and remodel our simulated cell walls by changing l_0 and θ_0. Our assumption that the preferred lengths of local cell wall segments l_0 only *increase* is reminiscent of the classic Lockhardt model of plant cell growth [39], where cell walls plastically deform and only grow when a threshold pressure is met. Through large variations of parameter space, we have found that the 13 parameters in our model (table 1) are all necessary to robustly grow plant cells in this way while simultaneously generating porous, mechanically stable cell networks.

As these growth rules induce applied stresses, relaxing stresses will lead to cell shape change and tissue growth. Therefore, after each stress step, we relax the total *enthalpy* $H = U + P_0 A$ for simulation domain area A at constant pressure $P_0 > 0$ and potential energy U. The presence of a positive pressure $P_0 > 0$ at the simulation boundary mimics the compressive effect that other tissues, such as the palisade mesophyll and epidermis, would have on the expanding spongy mesophyll. By using a modified version of the FIRE energy minimization algorithm ([40], see electronic supplementary material, section S3), a local minimum of the potential energy is found at a fixed pressure P_0. By finding a minimum of the enthalpy H instead of the potential energy U, the simulation domain area A will fluctuate to maintain the pressure at P_0. Maintaining a positive tissue pressure throughout a plant's life cycle is important in both individual cells and developing tissues [29,33,41,42].

A typical developmental trajectory for a simulation of six DP cells shows the changes in domain size, cell area and cell shape that occur (figure 2*e*, see also electronic supplementary material, supplementary movie). We show that the packing fraction

$$\phi = \frac{\sum_\mu a_\mu}{A} \tag{2.6}$$

is a monotonically decreasing function during the simulation (figure 2*g*). Note that the porosity, or fraction of air space in the simulation, is simply $1 - \phi$ and grows monotonically. It is important to note that the rate of packing fraction decrease

Table 1. Table of model parameters. Appendices (that provide a more complete description) are listed next to parameters that are not defined fully in the main text. Units of 1 signify dimensionless quantities. In the final column, numbers in parentheses indicate the values of the parameters in the simulation in figures 2 and 3. We show in figures 4 and 5 that the values selected for ϵ_b, β, Δa and λ are nearly optimal for recapitulating the developmental trajectory of spongy mesophyll in *A. thaliana*.

symbol	meaning	units	value
ϵ_a	area elasticity	energy unit	1
ϵ_l	perimeter elasticity	ϵ_a	1
ϵ_c	contact elasticity	ϵ_a	1
ϵ_b	bending elasticity	ϵ_a	10^{-2} – 1 (0.4)
$\mathcal{A}_{\max}$	shape parameter limit	$n\pi^{-1}\tan(n^{-1}\pi)$	3
β (electronic supplementary material, section S2)	inverse effective adhesion temperature	ϵ_a^{-1}	20–1000 (100)
r^* (electronic supplementary material, section S2)	relative bond fracture length	σ	2–4 (2.4)
Δa (electronic supplementary material, section S3)	cell area growth increment	ρ^2	10^{-4} – 0.75 (0.5)
λ (electronic supplementary material, section S3)	void perimeter growth scale	$n^{-1}\rho^{-2}\,p\Delta a$	1–10 (5)
c_L (electronic supplementary material, section S3)	perimeter growth regularization	1	0–1 (0.5)
c_B (electronic supplementary material, section S3)	scale of curvature change	$n^{-1}\rho^{-3}\,p\Delta a$	1–10 (4)
$\theta_{0,\min}$ (electronic supplementary material, section S3)	minimum bending angle	rads.	$-\pi/4$ – 0 ($-\pi/10$)
P_0	boundary pressure	$\epsilon_a\rho^{-2}$	10^{-7} – 0.1 (10^{-3})

is not stipulated in the model, such as via constant strain on the domain area that is set to be larger than the cell growth rate. Rather, the decrease in ϕ (figure 2*e*) is due entirely to the growth of void-facing perimeter segments and changes to boundary curvatures coupled to the constant-pressure boundary condition. That is, the decrease in ϕ (i.e. increase in $1-\phi$) *emerges* purely from localized cell stresses.

2.2. Simulations match cell shapes in experiments

The decrease in packing fraction of the tissue while maintaining a constant, positive pressure indicates that the DP model captures essential, qualitative features of spongy mesophyll development. In figure 3, we show that the model also recapitulates *quantitative* features of spongy mesophyll development. To quantify and compare cell shapes, we measure the cell *asphericity* or shape parameter,

$$\mathcal{A} = \frac{p^2}{4\pi a}, \tag{2.7}$$

where p and a are a given cell's (or cell projection's) perimeter and area, respectively. $\mathcal{A} = 1$ for circles and $\mathcal{A} > 1$ for all other two-dimensional shapes, e.g. $\mathcal{A} = 1.1$ for a regular hexagon and $\mathcal{A} = 1.65$ for an equilateral triangle. The average shape parameter of cell projections from *A. thaliana* leaves at varying developmental stages corresponded closely to the average $\mathcal{A}$ of cells in the developmental simulation shown in figure 2, changing from dense tissues early in development [23] to more porous tissues as the tissue matures (figure 3*a*). We quantified the agreement between the results from simulations and experiments using the root-mean-square deviation (RMSD) of the cell shape parameter,

$$\delta\mathcal{A} = \sqrt{\frac{\sum_{k=1}^{m}(\mathcal{A}_k^{\mathrm{sim}} - \mathcal{A}_k^{\mathrm{exp}})^2}{m}}, \tag{2.8}$$

where the kth experimental data point $\mathcal{A}_k^{\mathrm{exp}}$ can be compared with the simulation data point $\mathcal{A}_k^{\mathrm{sim}}$ with the most similar ϕ, and we average over $m = 9$ experimental time points. Over the full range of packing fraction for which we have experimental data, there was less than 4% deviation in $\mathcal{A}$ between simulations and experiments.

The DP model was also able to recapitulate and explain the transient decline in the shape parameter from $\mathcal{A} \approx 1.15$ to $\mathcal{A} \approx 1.05$ during the initial stages of *A. thaliana* leaf development (figure 3*c*). Cells are initially convex and confluent, and therefore, they must have a shape parameter of $\mathcal{A} \approx 1.15$ [31]. Because cell areas always grow but cells can grow their perimeter only near void space, cell perimeters do not grow when void space is rare. Thus, the cell perimeter does not grow in early stages, and $\mathcal{A}$ must decrease. However, as cells now prefer to be circular, pore space *must* open up as circular shapes cannot tile a plane. Once void space has sufficiently increased, cells can now grow their perimeters near voids and eventually $\mathcal{A}$ begins to increase. Our model captures and explains the emergence of non-monotonic behaviour of the shape parameter $\mathcal{A}$ during development despite monotonic decreases in the packing fraction ϕ.

The model succeeded in capturing key dynamics of the developing spongy mesophyll tissue. First, it recovered the non-monotonic behaviour of $\mathcal{A}$ in early developmental stages, suggesting that our assumptions regarding spongy mesophyll cell growth and interactions are valid. Second, the model accurately captured how adhesive, individual cells drive the opening of pore spaces. Third, the model successfully reproduced average shapes of mature cells at low packing fraction, down to $\phi \approx 0.5$ (figure 3). For this comparison, we calculated the average $\mathcal{A}$ of individual spongy mesophyll cells that had been segmented from X-ray microcomputed tomographic (microCT) scans of mature *A. thaliana* leaves. Together, these observations indicate that the features of the DP cell model are sufficient to reproduce several important quantitative and qualitative aspects of mesophyll development from the earliest stages of development to maturity.

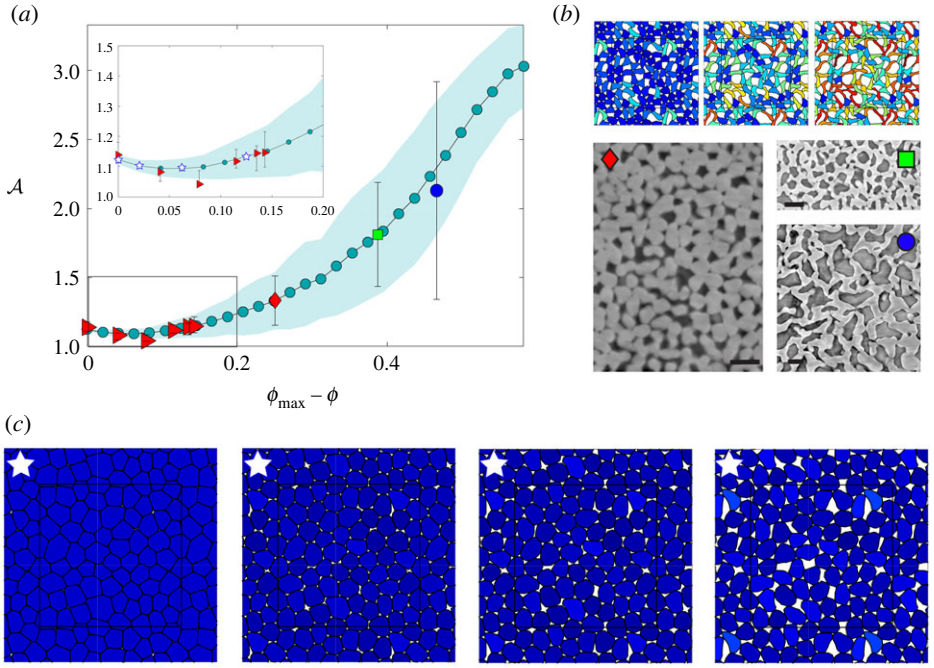

Figure 3. Comparison between simulations of the DP model of spongy mesophyll development and experimental observations. (*a*) Cell shape parameter $\mathcal{A}$ plotted against $\phi_{max} - \phi$ for a typical developmental trajectory from simulations (green circles, same as figure 2) and experimental characterization of two-dimensional cell shape projections in *Arabidopsis* at various packing fractions. Simulation error bars (green shaded area) represent the standard deviation in cell shape computed across 10 independent simulations. $\phi_{max} = 1$ for experiments, and 0.975 for simulations. Red triangles are from two-dimensional projections reported in [23], and the other markers represent $\mathcal{A}$ of cell projections from segmented microCT scans. The inset is a zoom-in of $\mathcal{A}$ versus $\phi_{max} - \phi$ to highlight the comparison with early developmental stages. (*b*) Simulation snapshots (top row) and microCT scans (bottom row, greyscale) shown at similar packing fractions. Each scan is labelled by the corresponding plot marker in (*a*), and simulations decrease in ϕ from left to right. Scale bars in each microCT scan are 50 µm. (*c*) Snapshots of simulations at low ϕ (corresponding to stars in the inset to (*a*)), decreasing in packing fraction from left to right. In (*b*) and (*c*), cell colour indicates $\mathcal{A}$ using the colourbar in figure 2*e*, and the simulation boundary is periodic and drawn as a black square.

2.3. Sensitivity of network formation to parameter variation

The agreement between the structural properties of spongy mesophyll tissue and of our model results indicates that the localized growth of cell perimeters near voids, cell adhesion and constant boundary pressure can indeed drive the self-assembly of the spongy mesophyll. We further tested the robustness of morphogenesis by characterizing how the structural properties of the tissue change with variation in the model parameters. In particular, we were interested in understanding the range of parameters that can recapitulate *A. thaliana* development and whether the packing fraction consistently decreases for any set of model parameters. Addressing these questions is important not only for determining the relevant parameter regime for comparison with spongy mesophyll in *A. thaliana* but also for understanding whether the development of the spongy mesophyll in other species can be described by this model [16].

To probe the sensitivity of the model, we varied two parameters at a time while setting all other model parameters to be similar to those used in figures 2 and 3. Comparisons of the average shape parameter $\mathcal{A}$ of simulations with experimental observations were split into early (i.e. $\delta\mathcal{A}_{early}$) and late (i.e. $\delta\mathcal{A}_{late}$) developmental stages, with the first $m = 6$ experimental data points (red triangles in figure 3) used to calculate $\delta\mathcal{A}_{early}$ and the last $m = 3$ data points (other symbols in figure 3) used to calculate $\delta\mathcal{A}_{late}$. We also calculated the cumulative compaction $\Delta\phi_+$, which we define as follows:

$$\Delta\phi_+ = \sum_{f=1}^{N_F} (\phi_{f+1} - \phi_f)\Theta(\phi_{f+1} - \phi_f). \tag{2.9}$$

This quantity tracks the total amount of compaction across a simulation with N_F frames, as the Heaviside step function enforces a sum over only positive changes in ϕ between frame f and $f+1$. In figure 4*a*, we plot $\Delta\phi_+$ as well as the average number of cell–cell contacts, z, at the simulation snapshots closest to $\phi = 0.5$.

First, we tested how varying Δa, the rate of areal growth, and λ, the rate of void-facing perimeter growth, influences mesophyll network formation (figure 4). RMSDs of $\delta\mathcal{A}_{early}$ and $\delta\mathcal{A}_{late}$ were minimized in the region where $\Delta a \sim 0.5$ and $\lambda \sim 5$ (green hexagon), with significant deviations from *A. thaliana* mesophyll in almost all other regions of parameter space. While any value of Δa led to low $\delta\mathcal{A}$ when $\lambda = 5$, low values of Δa led to developmental trajectories with increasing packing fraction rather than decreasing packing fraction, as indicated by $\Delta\phi_+$. Simulations with $\Delta a = 0.01$ and $\lambda = 5$ (red hexagon) show significant tissue compaction rather than expansion (figure 4*b*). Compaction probably results from buckling events during development, when a change in the cell shape parameter can make the system mechanically unstable. Simulations with lower Δa had fewer cell–cell contacts on average (figure 4*a*), suggesting that they were less stable. The reduction in z when $\Delta a < 0.01$ could result from there being more growth steps, which increased the probability of adhesive bond breakage. Thus, having a sufficient number of adhesive bonds and allowing sufficient growth to occur along void-facing perimeters are vital for the proper development of spongy mesophyll tissue in *A. thaliana*.

Second, we tested how varying the strength of the bending energy along cell boundaries ϵ_b (see equation (2.1)) and the inverse adhesion temperature β influence mesophyll network formation (figure 5). The inverse

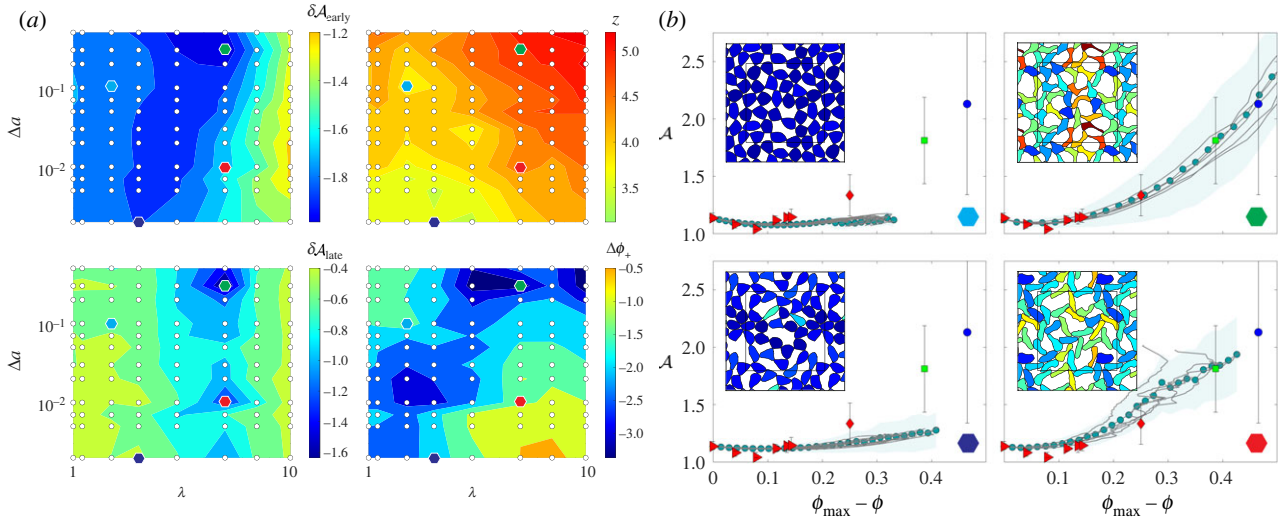

Figure 4. Effect of changing the areal growth Δa and void perimeter growth scale λ on the shape parameter, packing fraction and coordination number obtained in simulations. (*a*) Heatmaps of the RMSD of $\mathcal{A}$ from early developmental stages ($\mathcal{A}_{\text{early}}$, top-left), late developmental stages ($\mathcal{A}_{\text{late}}$, bottom-left), cumulative compaction ($\Delta\phi_+$, bottom-right) and mean coordination number closest to $\phi = 0.5$ (z, top-right). Colour represents $\log_{10}$ of each quantity, the values corresponding to each colour are indicated by the colourbars, and white circles represent values used to generate the heatmaps. In each heatmap, hexagons placed at (λ, Δa) = (1.5, 0.1) (cyan), (2, 0.002) (purple), (5, 0.01) (red) and (5, 0.5) (green) highlight exemplary simulations shown in (*b*). (*b*) Plots of $\mathcal{A}$ averaged over cells for each individual simulation (grey lines) and an ensemble average over five independent simulations (green circles) with shading denoting the standard deviation. Hexagons in the lower right corners indicate the particular ensemble parameters (i.e. Δa and λ) highlighted in (*a*). Each image in (*b*) shows the simulation frame closest to $\phi_{\max} - \phi = 0.465$, i.e. that of the latest stage experimental data point (blue circle in figure 3*a*,*b*). In each inset, cell colour denotes $\mathcal{A}$ as defined in the colourbar of figure 2*e*. Other parameters (defined in table 1) for these simulations are $\epsilon_b = 0.4$, $\beta = 100$, $h = 2.4$, $c_L = 0.5$, $c_B = 4$, $\theta_{0,\min} = -3\pi/20$ and $P_0 = 10^{-6}$.

adhesion temperature β defines the conditions when bonds break, with $\beta \to 0$ meaning that any stretched bond will break and $\beta \to \infty$ meaning that only bonds with energy $U_c > U_0$ will break (figure 2*d*). In electronic supplementary material, section S2, we show that changing U_0 by varying the breaking distance r^* does not dramatically affect the outcome of our simulations.

Our sensitivity testing reveals that β and ϵ_b must be sufficiently large to generate the correct self-assembly of *A. thaliana*-like cell networks (figure 5*a*). While the heatmap of $\delta\mathcal{A}_{\text{early}}$ suggests that β has little effect on *A. thaliana*-like mesophyll development at low ϕ, only a small fraction of simulations with large ϵ_b and large β generated correct cell shapes towards the end of development, indicating how developmental progression causes parameter space contraction. Furthermore, decreasing β, thus losing adhesive contacts, causes tissue compaction during development. This compaction probably occurs due to buckling events during development, where cell perimeters grow into void space rather than provide scaffolding for the growing pore spaces. One can see an example of buckled cells at higher densities in the high tissue pressure case in figure 6.

These sensitivity tests indicate that generating stable networks without significant buckling events requires both rigid cells *and* adhesive contacts (figures 4 and 5). As void perimeter growth drives tissue boundary growth in our model, stronger cell perimeter length segments provide rigid scaffolds that can more effectively open pore spaces. However, larger values of β, which reduce the likelihood of breaking bonds between cells, also lead to the consistent formation of stable, porous cell networks. Successful development of the spongy mesophyll tissue requires that stressed adhesive contacts collectively push the boundary *outwards*. That stressed, adhesive bonds can drive expansion seems counter-intuitive. However, pre-stressed bonds can rigidify floppy spring networks [32,43,44]. Developing cell networks, therefore, may locally rigidify some regions of the tissue with stretched bonds in order to push outwards, rather than pull inwards, on the tissue boundary.

Self-organization of mechanical stresses is vital to the correct opening of pore space during spongy mesophyll development. To test the effect of bulk mechanical stress on this process, we varied the external boundary pressure P_0 and measured its effect on the structural properties of the tissue during development. Increasing pressure either negligibly affected the simulation results or caused compaction of the tissue (figure 6). When the imposed boundary pressure $P_0 \lesssim 10^{-3}$, the structural properties during development were weakly affected by changes in P_0 (for example, tissue microstructures were virtually identical when $P_0 = 10^{-7}$ and 10^{-5}). However, increasing the external pressure above $P_0 = 10^{-3}$ caused the average cell shape parameter to increase more rapidly than that observed in *A. thaliana* and led to dramatic increases in the cumulative compaction $\Delta\phi_+$. For example, when $P_0 = 5 \times 10^{-2}$, the system compacts rather than expands in later stages, with cells taking on extremely non-spherical shapes (figure 6). Under such high pressures, growing perimeter segments are unable to push out on the boundary and instead buckle into the void space. The resultant tissue does not expand as much and can even begin to compact, highlighting the importance of pressure regulation in spongy mesophyll development. Because cell perimeters continue to grow, cells assume biologically unrealistic shapes with extremely large values of $\mathcal{A}$.

The physiological units of the boundary pressure can be obtained by approximating the energy cost for volume changes of hypothetical three-dimensional cells. For a three-dimensional cell with volume V, the energy due to changes

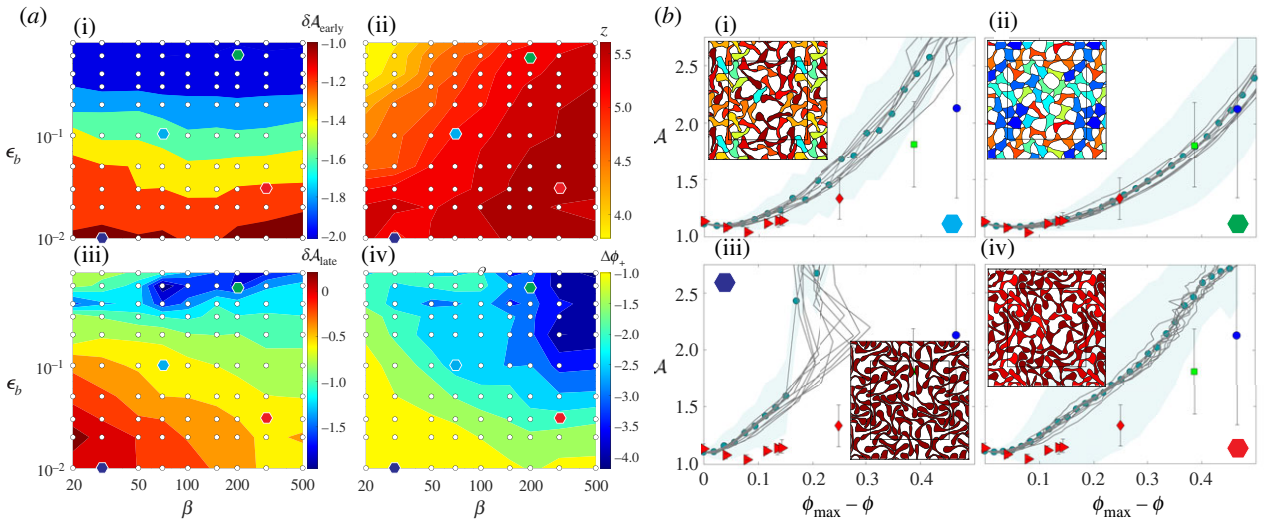

Figure 5. Effect of changing the inverse adhesion temperature β and bending energy ϵ_b on the shape parameter, packing fraction and coordination number obtained in simulations. (*a*) Heatmaps of the shape parameter RMSD from early developmental stages ($\mathcal{A}_{\text{early}}$, (i)) and late developmental stages ($\mathcal{A}_{\text{late}}$, (iii)), cumulative compaction ($\Delta\phi_+$, iv), and mean coordination closest to $\phi = 0.5$ (z, (ii)). The colour represents $\log_{10}$ of each quantity, and the values corresponding to each colour are shown in the colourbars. Hexagons placed at $(\beta, \epsilon_b) = (70, 0.1)$ (cyan), (30, 0.01) (purple), (300, 0.03) (red) and (200, 0.6) (green) highlight four exemplary simulations, shown in (*b*). (*b*) Plots of $\mathcal{A}$ versus $\phi_{max} - \phi_{max}$ (with snapshots from the simulations in the insets) for the highlighted points in the (ϵ_b, β) parameter space (grey lines and green circles represent the same as in figure 4). In each inset, cell colour denotes $\mathcal{A}$ as defined in the colourbar of figure 2*e*. Other parameters (defined in table 1) for these simulations are $r^* = 2.4\sigma$, $\Delta a = 0.5$, $\lambda = 5$, $c_L = 0.5$, $c_B = 4$, $\theta_{0,\text{min}} = -3\pi/20$ and $P_0 = 10^{-7}$.

in volume would be

$$U_{3D} = \frac{\epsilon}{2}\left(\frac{V}{V_0} - 1\right)^2, \tag{2.10}$$

where V_0 is a cell's preferred volume and ϵ sets the energy cost for volume fluctuations. If we assume that U_{3D} is the dominant contribution to isotropic compression, each cell's bulk modulus is

$$B \approx -V_0 \frac{\partial^2 U_{3D}}{\partial V^2} = \frac{\epsilon}{V_0}. \tag{2.11}$$

If we extend our two-dimensional cells into the third dimension, we can approximate $V_0 \sim a_0^{3/2}$ and $\epsilon = \epsilon_a$, that is, the energy of area deviations. Since ϵ_a and $\sqrt{a_0}$ are the units for energy and length scales, the cell bulk modulus is then the unit of pressure in our simulations. If we assume that plant cells have an instantaneous bulk modulus set by the bulk modulus of water, the unit of pressure in our simulations should be approximately 1 GPa. The internal turgor pressure in spongy mesophyll cells has been observed to be approximately 10^{-1} MPa [29,45–48], which is consistent with the scale of cell turgor pressure in other tissues [33,49], and corresponds to 10^{-4} in the units of our simulations. Thus, our observation that development is affected by the boundary pressure when $P_0 \gtrsim 10^{-3}$ suggests that the *tissue* pressure must not exceed the *cell* turgor pressure by a factor of 10 or more. While we know of no measurements of spongy mesophyll boundary pressure, this analysis provides a reasonable upper bound on the tissue pressure. That our model predicts an upper bound for P_0, but not a *lower* bound, suggests that mesophyll tissue could grow in the absence of a confining pressure. However, our model still vitally depends on the imposition of constant stress (even if this stress is small or near zero), as growth of a boundary at constant strain can lead to the presence of large fracture events and heterogenous void distribution, rather than smaller voids with a homogenous void distribution.

3. Discussion

In this article, we have presented a model of spongy mesophyll development using simulations of deformable polygons that illuminates key cell-level processes driving morphogenesis. This model is, to our knowledge, the first quantitative developmental model of the leaf mesophyll. Our model employs localized growth of cell perimeter to expand the tissue boundary, which is held at constant pressure, such that the internal tissue becomes more porous. This growth process allows tissues to be driven to highly porous states of packing fraction $\phi = 0.5$ or less, while remaining mechanically stable. The success of the model in recapitulating the developmental trajectory of the mean cell shape parameter $\mathcal{A}$ of *A. thaliana* from the earliest stages of development to maturity provides insights into the dynamics of mesophyll cell and tissue development. Furthermore, by varying model parameters, we found that maintaining adhesive contacts between cells and having cells that are sufficiently stiff are two vital components of the model that ensure correct spongy mesophyll development. Without either feature, cell buckling leads to compaction rather than expansion in response to cell growth.

The developmental trajectories produced by our model answer key questions about mesophyll development and airspace formation. First, mesophyll porosity can develop without cell death, relying entirely on cell expansion (expansigeny) [23]. The ability of our model to recapitulate *A. thaliana* mesophyll development suggests that the selective cell death is not required to generate developmental increases in mesophyll porosity, perhaps in contrast to airspace formation in other plant tissues [24]. Second, localizing cell wall growth to regions adjacent to airspace allows for both increasing cell asphericity and the expansion of intercellular airspace. If the cell growth was constant around the perimeter of cells, then cell shape change *per se* would be driven solely by mechanical stresses bending and stretching the cell wall. The cell wall expansion that is largely isolated to regions of the cell perimeter bordering airspace enables much more dramatic

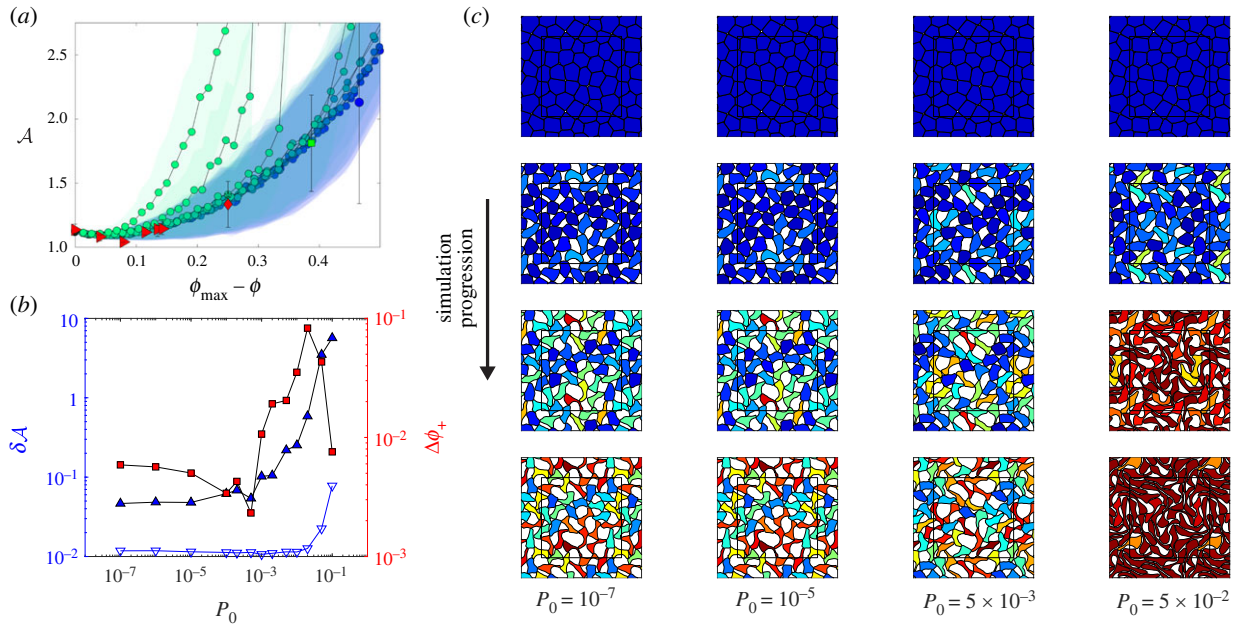

Figure 6. Effect of changing the boundary pressure P_0 on the structural properties during development in simulations. (*a*) Mean cell shape parameter $\mathcal{A}$ for simulations of 32 cells for P_0 between 10^{-7} and 10^{-1}, sorted from low (blue) to high (green). (*b*) The shape parameter RMSD ($\delta\mathcal{A}$, left axis, blue triangles) and cumulative compaction ($\Delta\phi_+$, right axis, red squares) for simulations at different P_0. Blue downward triangles denote $\delta\mathcal{A}_{early}$, and blue upward triangles denote $\delta\mathcal{A}_{late}$. (*c*) Snapshots of simulations at various pressures drawn using periodic boundary conditions, where the cell colour denotes $\mathcal{A}$ with the colourbar in figure 2. Snapshots are taken at the first frame (row 1, $\phi = 0.975$), and frames with ϕ values closest to those for the three microCT scans in figure 3*b*, i.e. $\phi =$ 0.75, 0.6 and 0.52. Other parameters for these simulations are $\epsilon_b = 0.4$, $\beta = 100$, $h = 2.4$, $\Delta a = 0.5$, $\lambda = 5$, $c_L = 0.5$, $c_B = 4$ and $\theta_{0,min} = -3\pi/20$.

changes in cell shape during development [23]. Third, we find that maintaining some adhesive bonds between cells and allowing others to break are vital for tissue stability and properly opening pore space during development. Bond breaking is important for airspace formation, since loss of cell–cell contact allows voids to open. Our model also demonstrates that losing too many adhesive bonds compromises tissue integrity and can stall or even reverse tissue expansion. Fourth, air space formation in the mesophyll need not depend on the epidermis pulling mesophyll cells apart. By maintaining constant pressure on the developing mesophyll, our model suggests that epidermal expansion can occur at the same rate as mesophyll expansion. Thus, this relatively simple model aligns with recent insights into mesophyll development in *A. thaliana* and highlights the features that are necessary for the spongy mesophyll to develop properly.

Similar to a recent computational model of epidermal development [5], our model is consistent with current understanding of the molecular underpinnings of mesophyll development. Consistent with our finding that epidermal expansion need not pull mesophyll cells apart to form the intercellular airspace, *A. thaliana* mutants that lack an epidermis nonetheless produce a porous mesophyll [50]. This finding reiterates the role of single cell behaviour and growth in driving mesophyll morphogenesis. Other features of our model, such as the preferred bending angle (θ_0) and cell adhesion (β), have known molecular cognates. The preferred bending angle could result from molecular processes that pattern cell growth, such as microtubules that form bands in different regions of mesophyll cells and drive cell wall reinforcement [22,24,51]. In particular, the observation that microtubules localize to void-facing surfaces in mesophyll cells [23] during development provides a possible molecular origin for active stresses driving boundary curvature changes. In addition, our model can capture important features in plant cell adhesion. In general, cells are adhered together by the middle lamella, and modification of middle lamella composition can alter cell–cell adhesion [28,34,52]. For example, methyl esterification, which is controlled by pectin methyl esterase, can alter adhesive contacts and make them more susceptible to breaking [28,34]. Thus, while our model of mesophyll development is purely mechanical, its parameters have known molecular and physiological underpinnings.

Our sensitivity tests provide additional insights into the robustness and potential diversity of mesophyll developmental trajectories. Many of the simulations using different parameter values produced stable structures, and some simulations produced tissues that had little-to-no buckling during development, but still possessed significant deviations in $\mathcal{A}$ compared with *A. thaliana* (e.g. the results for $\Delta a = 2 \times 10^{-3}$ and $\lambda = 2$ (purple hexagon) in figure 4*b*). These alternative trajectories may correspond to the developmental trajectories of the spongy mesophyll for other plant species. The spongy mesophyll is very diverse, most notably in porosity, which varies from approximately 25% to 75% among species and in cell size and shape [14,16,17]. If different parameter values in this model can recapitulate the developmental trajectories of other species, then studies of the landscape of possible phenotypes generated by our model could elucidate the biophysical basis of mesophyll diversity. In addition to the parameters explicitly defined in our model, other assumptions in our model could be relaxed to generate a greater diversity of developmental trajectories. For example, our implementation of the DP model assumes constant, i.e. ϕ-independent, growth rates. Would we obtain different dynamics for the structural properties of the spongy mesophyll if, for example, areal growth depended directly on the amount of void-facing cell surfaces? In addition to varying parameter values in the model, arresting mesophyll expansion at different points along the developmental trajectory

can produce an array of different mesophyll porosities and cell shapes (figure 2). Heterochronic changes, such as paedomorphosis—when mature individuals retain traits previously seen only in immature individuals of closely related species—commonly occur during speciation. Our model of mesophyll development recapitulates much of the cell shape diversity seen among species [16], suggesting that a single developmental trajectory can itself provide numerous possible mature phenotypes. Additional rules may be necessary for simulations to correspond to mesophyll phenotypes observed in other species, e.g. disordered, planar honeycomb lattices of cells [16]. Therefore, better experimental characterization of the structural changes during development for a variety of species is needed to better understand the range of possible phenotypes and to determine whether the DP model can describe them.

Our simulations do miss some quantitative details of spongy mesophyll development in *A. thaliana*. For example simulated values of $\mathcal{A}$ never quite reach the minimum value of $\mathcal{A} \approx 1.05$ observed in experimental data. The inability of the model to capture this particular feature may be due to the assumption of constant growth rates, whereas real spongy mesophyll cells may have more complex cell shape feedback mechanisms that drive this decrease in $\mathcal{A}$. Our simulations also contain more highly coordinated cells in the more porous stages of development than those in the experimental images. For example, the most porous experimental structure that we observed (i.e. the blue circle in figure 3*b*) has an average cell–cell coordination number $z = 3.5$. However, the simulated tissues with low $\delta\mathcal{A}_{\text{late}}$ typically have $z \sim 4.5$–5 even though the cell shapes are nearly identical to those in experiments (figures 3–5). One explanation for this discrepancy is that cells in real leaves are stabilized by out-of-plane contacts and require fewer contacts in the paradermal plane to remain mechanically stable. Extending our two-dimensional mesophyll model into three dimensions using deformable polyhedra [53] would be an advancement in understanding mesophyll development. Such an approach could incorporate the presence of other tissues, such as the palisade mesophyll, the epidermis and veins on the development of the spongy mesophyll. Nonetheless, the success of our relatively simple two-dimensional model in recapitulating the dynamics of spongy mesophyll development in the paradermal plane suggests that our model captures all of the fundamental biological mechanisms that control mesophyll development.

4. Methods and materials

4.1. Plant materials and growth condition

The seeds of transgenic *A. thaliana* Columbia-0 (Col-0) plants expressing RbcS1B:mKO-PIP2;1 [54] were sown on plates containing 1/2 MS salts, 1% sucrose and 1% agar and stratified at 4°C for 48 hours before moving to a growth cabinet set to 22°C, 16/8 h light/dark cycle. The first true leaves were used for imaging after their emergence from the bases of cotyledons.

4.2. Sample preparation and microscopy

For live cell imaging, the cotyledons were cut off to expose the young first true leaves after their emergence at 6–7 days after sowing, then the rest of seedlings were mounted in 20 µl perfluoroperhydrophenanthrene (PP11; Sigma 56919) within chambered coverglass (Nunc; Thermo Scientific 155360) and covered by a piece of 2–3 mm thick 0.7% phytagel containing 1% sucrose and 1/2 MS salts. All images were obtained via point-scan confocal microscopy (Zeiss LSM 880; Airyscan). mKusabira-Orange (mKO) excitation was performed using a 543 nm laser, and fluorescence was detected at 555–610 nm. During the imaging intervals, the samples were kept in the growth cabinet (22°C, 16/8 h light/dark cycle) inside covered glass Petri dishes with a moist paper towel to maintain humidity; meanwhile PP11 was added occasionally to prevent drying.

4.3. Image processing

Confocal Z-stacks were processed in ImageJ [55] and FluoRender [56]. Maximum intensity Z-projections were generated for each timepoint and used for subsequent analysis. The first layer of spongy mesophyll was used for analysis. When required, the inner layers were manually removed in FluoRender.

4.4. MicroCT imaging

For the two densest microCT scans shown in figure 3*b* (the source of the red diamond and green square data points), seeds of *A. thaliana* Col-0 were sown on moist filter paper in a Petri dish and stratified in a cold room at 4°C for 5 days. They were then left to germinate at room temperature under 200 µmol photosynthetic photon flux density(PPFD) $m^{-2}\,s^{-1}$ light. Once germinated, seedlings were transferred to individual pots of 8 cm diameter and height. Seedlings were then transferred to a climate-controlled room with 21/18°C day/*night temperature*, 60% relative humidity and 8 h photoperiod of 500 µmol PPFD $m^{-2}\,s^{-1}$. Plants were fertilized regularly using a complete liquid fertilizer solution. Plants were grown for approximately 6 weeks.

One healthy and fully grown plant was brought to the TOMCAT tomographic beamline X02DA of the Swiss Light Source at the Paul Scherrer Institute (Villigen, Switzerland). Of that plant, two leaves were included in this analysis: the youngest leaf (red diamond, figure 3*b*) large enough to be sampled (approx. 10–20 mm^2), as well as an older leaf (green square, figure 3*b*). Before scanning, the petiole of each leaf was cut into a thin strip 1.5 mm wide and up to 1.5 cm long in between apparent higher order veins and immediately wrapped in polyimide tape [14]. Each strip was scanned within 15 min of being prepared by imaging 1801 projections of 100 ms under a beam energy of 21 keV and magnified using a 20× objective, yielding a final voxel size of 0.325 µm (field of view: 832 × 832 × 624 µm). Projections were reconstructed using phase contrast enhancement [57], which provides a high contrast between the airspace and the mesophyll cells, sufficient to segment using a simple grey-value threshold.

For the most porous microCT scan shown in figure 3*b* (the source of the blue circle), seeds of *A. thaliana* Col-0 were plated onto wet filter paper and placed in a fridge at 4°C for cold treatment. One week later, seeds were moved to soil (Pro-Mix BX with biofungicide; Premier Horticulture Ltd, Rivière-du-Loup, Québec, Canada) and grown in growth chambers at Yale University (22°C, 60% humidity, 16 h photoperiod with 100 µmol $m^{-2}\,s^{-1}$ light). Plants were watered twice per week with fertilized water (Jack's 20-10-20 Peat-lite special; 200 ppm N). A fully expanded leaf was

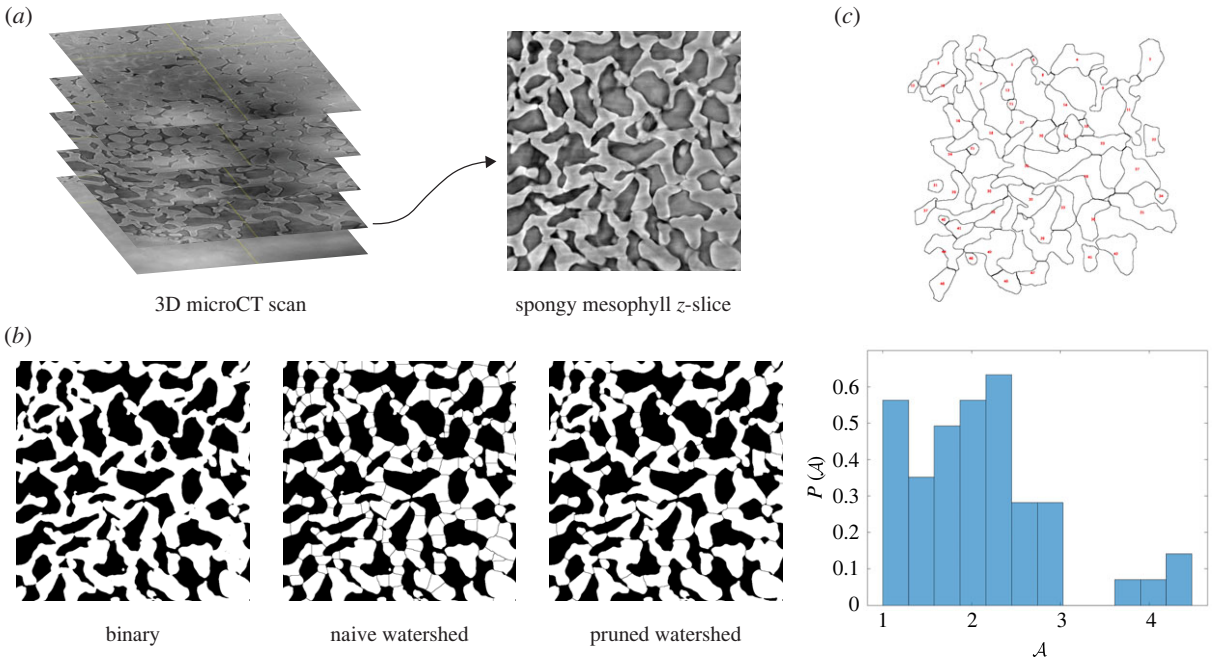

Figure 7. Process of segmenting spongy mesophyll cells from the original greyscale microCT data. (*a*) First, a single paradermal *z*-slice that represents the spongy mesophyll is selected. Here, we select the *z*-slice shown in figure 1*d*. (*b*) We then binarize, watershed and prune the image to obtain approximate boundaries for the two-dimensional cell projections. (*c*) We show the segmented cells, as well as the distribution of cell shape parameters $P(\mathcal{A})$. The mean of this distribution is $\overline{\mathcal{A}} = 2.13$.

excised from a Col-0 plant and placed inside a plastic bag with wet paper towels, then transported to the Advanced Light Source (ALS) at the Lawrence Berkeley National Lab (Berkeley, CA). A sample was prepared by cutting out a small (approx. 3 mm wide and approx. 10 mm long) section at the midpoint of the leaf halfway between the midrib and leaf margin and mounting this section between pieces of Kapton Tape (E.I. du Pont de Nemours and Company, Wilmington, DE, USA). Preparation was performed less than 30 min before scanning to avoid desiccation. The sample was mounted in a sample holder and scanned at the ALS using continuous tomography mode with a 10× objective lens, capturing 1025 projection images at 21 keV. An image stack was reconstructed following the previous work [58]. The reconstructed stack was cropped to remove areas damaged by cutting or dehydration.

4.5. Manual cell segmentation

For each microCT dataset shown in figure 3, we performed a binarization and watershed procedure in ImageJ as outlined in figure 7. Once a representative *z*-slice of the spongy mesophyll was selected from a fully three-dimensional microCT scan, we binarized the image and used a watershed algorithm [59] to identify cell boundaries. However, we found that initial boundaries drawn by the watershed algorithm divided some highly concave cells in regions where no clear boundaries can be seen in the original greyscale image. Therefore, we manually pruned extraneous boundaries by comparing each naive watershed boundary with the greyscale images and flipped void pixels to cell pixels for any incorrect boundaries. Once all extraneous boundaries were removed, we computed the shape parameter $\mathcal{A} = p^2/4\pi a$ for each remaining binary region of cell pixels with perimeters p and areas a. In figure 7, we show the distribution of cell shapes gleaned by this method from the most porous experimental snapshot (i.e. the blue circle in figure 3*b*).

Data accessibility. All experimental data (i.e. microCT scans) and data for the simulation shown in figures 2 and 3 can be accessed at an OSF data repository created for this manuscript, which can be found at https://doi.org/10.17605/OSF.IO/C4RBM [60]. All code used for simulations and data processing can be found in the github repository https://github.com/jacktreado/dpm.

The data are provided in electronic supplementary material [61].

Authors' contributions. J.D.T.: conceptualization, formal analysis, investigation, software, visualization, writing—original draft and writing—review and editing; A.B.R.: conceptualization, data curation, funding acquisition, investigation, supervision and writing—review and editing; G.T.-R.: data curation, formal analysis and writing—review and editing; L.Z.: data curation; C.A.: data curation; C.R.B.: conceptualization, data curation, funding acquisition, investigation, supervision and writing—review and editing; M.D.S.: conceptualization, supervision and writing—review and editing; C.S.O.: conceptualization, funding acquisition, investigation, supervision, writing—original draft and writing—review and editing.

All authors gave final approval for publication and agreed to be held accountable for the work performed therein.

Conflict of interest declaration. We declare we have no competing interests.

Funding. J.D.T., A.B.R., C.R.B. and C.S.O. were supported by NSF grant no. BMMB-2029756. G.T.-R. was supported by the Austrian Science Fund (FWF), projects M2245, and by the Vienna Science and Technology Fund (WWTF), project LS19-013. This work was also supported by the High Performance Computing facilities operated by Yale's Center for Research Computing. The Advanced Light Source is supported by the Director, Office of Science, Office of Basic Energy Science, of the US Department of Energy under contract no. DE-AC02- 05CH11231.

Acknowledgements. We would like to thank Dr Anne Bonnin of the TOMCAT beamline X02DA of the Swiss Light Source, as well as Mona Nazari and Dr Leila Fletcher, for assistance during microCT sample preparation and scanning.

References

1. Avery GS. 1933 Structure and development of the tobacco leaf. *Am. J. Bot.* **20**, 565–592. (doi:10.1002/j.1537-2197.1933.tb08913.x)
2. Green PB. 1965 Pathways of cellular morphogenesis: a diversity in *Nitella*. *J. Cell Biol.* **27**, 343–363. (doi:10.1083/jcb.27.2.343)
3. Seago James LJ, Marsh LC, Stevens KJ, Soukup A, Votrubová O, Enstone DE. 2005 A re-examination of the root cortex in wetland flowering plants with respect to aerenchyma. *Ann. Bot.* **96**, 565–579. (doi:10.1093/aob/mci211)
4. Ivakov A, Persson S. 2013 Plant cell shape: modulators and measurements. *Front. Plant Sci.* **4**, 439. (doi:10.3389/fpls.2013.00439)
5. Sapala A *et al.* 2018 Why plants make puzzle cells, and how their shape emerges. *eLife* **7**, e32794. (doi:10.7554/eLife.32794)
6. Antreich SJ, Xiao N, Huss JC, Horbelt N, Eder M, Weinkamer R, Gierlinger N. 2019 The puzzle of the walnut shell: a novel cell type with interlocked packing. *Adv. Sci.* **6**, 1900644. (doi:10.1002/advs.201900644)
7. Roddy AB *et al.* 2020 The scaling of genome size and cell size limits maximum rates of photosynthesis with implications for ecological strategies. *Int. J. Plant Sci.* **181**, 75–87. (doi:10.1086/706186)
8. Hamant O *et al.* 2008 Developmental patterning by mechanical signals in *Arabidopsis*. *Science* **322**, 1650–1655. (doi:10.1126/science.1165594)
9. Sampathkumar A, Yan A, Krupinski P, Meyerowitz EM. 2014 Physical forces regulate plant development and morphogenesis. *Curr. Biol.* **24**, R475–R483. (doi:10.1016/j.cub.2014.03.014)
10. Vőfély RV, Gallagher J, Pisano GD, Bartlett M, Braybrook SA. 2019 Of puzzles and pavements: a quantitative exploration of leaf epidermal cell shape. *N. Phytol.* **221**, 540–552. (doi:10.1111/nph.15461)
11. Roeder AHK, Tarr PT, Tobin C, Zhang X, Chickarmane V, Cunha A, Meyerowitz EM. 2011 Computational morphodynamics of plants: integrating development over space and time. *Nat. Rev. Mol. Cell Biol.* **12**, 265–273. (doi:10.1038/nrm3079)
12. Boudon F, Chopard J, Ali O, Gilles B, Hamant O, Boudaoud A, Traas J, Godin C. 2015 A computational framework for 3D mechanical modeling of plant morphogenesis with cellular resolution. *PLoS Comput. Biol.* **11**, 1–16. (doi:10.1371/journal.pcbi.1003950)
13. Lundgren MR *et al.* 2019 Mesophyll porosity is modulated by the presence of functional stomata. *Nat. Commun.* **10**, 2825. (doi:10.1038/s41467-019-10826-5)
14. Théroux-Rancourt G *et al.* 2021 Maximum CO_2 diffusion inside leaves is limited by the scaling of cell size and genome size. *Proc. R. Soc. B* **288**, 20203145. (doi:10.1098/rspb.2020.3145)
15. Scott FM, Schroeder MR, Turrell FM. 1948 Development, cell shape, suberization of internal surface, and abscission in the leaf of the Valencia orange, *Citrus sinensis*. *Botanical Gazette* **109**, 381–411. (doi:10.1086/335493)
16. Borsuk AM, Roddy AB, Théroux-Rancourt G, Brodersen CR. 2022 Structural organization of the spongy mesophyll. *N. Phytol.* **234**, 946–960. (doi:10.1111/nph.17971)
17. Théroux-Rancourt G, Voggeneder K, Tholen D. 2020 Shape matters: the pitfalls of analyzing mesophyll anatomy. *N. Phytol.* **225**, 2239–2242. (doi:10.1111/nph.16360)
18. Terashima I, Miyazawa SI, Hanba YT. 2001 Why are sun leaves thicker than shade leaves?—Consideration based on analyses of CO_2 diffusion in the leaf. *J. Plant Res.* **114**, 93–105. (doi:10.1007/PL00013972)
19. Evans JR, Vogelmann TC. 2003 Profiles of ^{14}C fixation through spinach leaves in relation to light absorption and photosynthetic capacity. *Plant, Cell & Environ.* **26**, 547–560. (doi:10.1046/j.1365-3040.2003.00985.x)
20. Lehmeier C *et al.* 2017 Cell density and airspace patterning in the leaf can be manipulated to increase leaf photosynthetic capacity. *Plant J.* **92**, 981–994. (doi:10.1111/tpj.13727)
21. Psaras GK, Rhizopoulou S. 1995 Mesophyll structure during leaf development in *Ballota acetabulosa*. *N. Phytol.* **131**, 303–309. (doi:10.1111/j.1469-8137.1995.tb03066.x)
22. Panteris E, Galatis B. 2005 The morphogenesis of lobed plant cells in the mesophyll and epidermis: organization and distinct roles of cortical microtubules and actin filaments. *N. Phytol.* **167**, 721–732. (doi:10.1111/j.1469-8137.2005.01464.x)
23. Zhang L, McEvoy D, Le Y, Ambrose C. 2021 Live imaging of microtubule organization, cell expansion, and intercellular space formation in *Arabidopsis* leaf spongy mesophyll cells. *Plant Cell* **33**, 623–641. (doi:10.1093/plcell/koaa036)
24. Whitewoods CD. 2021 Riddled with holes: understanding air space formation in plant leaves. *PLoS Biol.* **19**, 1–13. (doi:10.1371/journal.pbio.3001475)
25. Wuyts N, Palauqui JC, Conejero G, Verdeil JL, Granier C, Massonnet C. 2010 High-contrast three-dimensional imaging of the *Arabidopsis* leaf enables the analysis of cell dimensions in the epidermis and mesophyll. *Plant Methods* **6**, 17. (doi:10.1186/1746-4811-6-17)
26. Kalve S, Fotschki J, Beeckman T, Vissenberg K, Beemster GTS. 2014 Three-dimensional patterns of cell division and expansion throughout the development of *Arabidopsis thaliana* leaves. *J. Exp. Bot.* **65**, 6385–6397. (doi:10.1093/jxb/eru358)
27. Harwood R, Théroux-Rancourt G, Barbour MM. 2021 Understanding airspace in leaves: 3D anatomy and directional tortuosity. *Plant, Cell Environ.* **44**, 2455–2465. (doi:10.1111/pce.14079)
28. Daher FB, Braybrook SA. 2015 How to let go: pectin and plant cell adhesion. *Front. Plant Sci.* **6**, 523. (doi:10.3389/fpls.2015.00523)
29. Zimmermann U, Hüsken D, Schulze ED. 1980 Direct turgor pressure measurements in individual leaf cells of *Tradescantia virginiana*. *Planta* **149**, 445–453. (doi:10.1007/BF00385746)
30. Eng RC, Sampathkumar A. 2018 Getting into shape: the mechanics behind plant morphogenesis. *Curr. Opin Plant Biol.* **46**, 25–31. (doi:10.1016/j.pbi.2018.07.002)
31. Boromand A, Signoriello A, Ye F, O'Hern CS, Shattuck MD. 2018 Jamming of deformable polygons. *Phys. Rev. Lett.* **121**, 248003. (doi:10.1103/PhysRevLett.121.248003)
32. Treado JD, Wang D, Boromand A, Murrell MP, Shattuck MD, O'Hern CS. 2021 Bridging particle deformability and collective response in soft solids. *Phys. Rev. Mater.* **5**, 055605. (doi:10.1103/PhysRevMaterials.5.055605)
33. Niklas KJ, Spatz HC. 2012 *Plant physics*. Chicago, IL: University of Chicago Press.
34. Lionetti V, Cervone F, De Lorenzo G. 2015 A lower content of de-methylesterified homogalacturonan improves enzymatic cell separation and isolation of mesophyll protoplasts in *Arabidopsis*. *Phytochemistry* **112**, 188–194. (doi:10.1016/j.phytochem.2014.07.025)
35. Sifton HB. 1945 Air-space tissue in plants. *Botanical Rev.* **11**, 108–143. (doi:10.1007/BF02861138)
36. Gao GJ, Bławzdziewicz J, O'Hern CS. 2006 Frequency distribution of mechanically stable disk packings. *Phys. Rev. E* **74**, 061304. (doi:10.1103/PhysRevE.74.061304)
37. Rhizopoulou S, Psaras GK. 2003 Development and structure of drought–tolerant leaves of the mediterranean shrub *Capparis spinosa* L. *Ann. Bot.* **92**, 377–383. (doi:10.1093/aob/mcg149)
38. Harwood R, Goodman E, Gudmundsdottir M, Huynh M, Musulin Q, Song M, Barbour MM. 2020 Cell and chloroplast anatomical features are poorly estimated from 2D cross-sections. *N. Phytol.* **225**, 2567–2578. (doi:10.1111/nph.16219)
39. Goriely A. 2017 Growing on a line. In *The mathematics and mechanics of biological growth* (eds SS Antam, L Greengard, PJ Holmes), pp. 63–96. New York, NY: Springer.
40. Bitzek E, Koskinen P, Gähler F, Moseler M, Gumbsch P. 2006 Structural relaxation made simple. *Phys. Rev. Lett.* **97**, 170201. (doi:10.1103/PhysRevLett.97.170201)
41. Zonia L, Müller M, Munnik T. 2006 Hydrodynamics and cell volume oscillations in the pollen tube apical region are integral components of the biomechanics of *Nicotiana tabacum* pollen tube growth. *Cell Biochem. Biophys.* **46**, 209–232. (doi:10.1385/CBB:46:3:209)
42. Kroeger JH, Zerzour R, Geitmann A. 2011 Regulator or driving force? The role of turgor pressure in oscillatory plant cell growth. *PLoS ONE* **6**, 1–12. (doi:10.1371/journal.pone.0018549)
43. Jacobs DJ, Thorpe MF. 1996 Generic rigidity percolation in two dimensions. *Phys. Rev. E* **53**, 3682. (doi:10.1103/PhysRevE.53.3682)

44. Donev A, Connelly R, Stillinger FH, Torquato S. 2007 Underconstrained jammed packings of nonspherical hard particles: ellipses and ellipsoids. *Phys. Rev. E* **75**, 051304. (doi:10.1103/PhysRevE.75.051304)
45. Frensch J, Schulze ED. 1988 The effect of humidity and light on cellular water relations and diffusion conductance of leaves of *Tradescantia virginiana* L. *Planta* **173**, 554–562. (doi:10.1007/BF00958969)
46. Nonami H, Schulze ED. 1989 Cell water potential, osmotic potential, and turgor in the epidermis and mesophyll of transpiring leaves. *Planta* **177**, 35–46. (doi:10.1007/BF00392152)
47. Thürmer F, Zhu JJ, Gierlinger N, Schneider H, Benkert R, Geßner P, Herrmann B, Bentrup FW, Zimmerniann U. 1999 Diurnal changes in xylem pressure and mesophyll cell turgor pressure of the liana *Tetrastigma voinierianum*: the role of cell turgor in long-distance water transport. *Protoplasma* **206**, 152–162. (doi:10.1007/BF01279262)
48. Roddy AB, Jiang GF, Cao K, Simonin KA, Brodersen CR. 2019 Hydraulic traits are more diverse in flowers than in leaves. *N. Phytol.* **223**, 193–203. (doi:10.1111/nph.15749)
49. Kutschera U, Niklas K. 2007 The epidermal-growth-control theory of stem elongation: an old and a new perspective. *J. Plant Physiol.* **164**, 1395–1409. (doi:10.1016/j.jplph.2007.08.002)
50. Abe M, Katsumata H, Komeda Y, Takahashi T. 2003 Regulation of shoot epidermal cell differentiation by a pair of homeodomain proteins in *Arabidopsis*. *Development* **130**, 635–643. (doi:10.1242/dev.00292)
51. Panteris E, Apostolakos P, Galatis B. 1993 Microtubule organization, mesophyll cell morphogenesis, and intercellular space formation in *Adiantum capillus veneris* leaflets. *Protoplasma* **172**, 97–110. (doi:10.1007/BF01379367)
52. Bidhendi AJ, Geitmann A. 2015 Relating the mechanics of the primary plant cell wall to morphogenesis. *J. Exp. Bot.* **67**, 449–461. (doi:10.1093/jxb/erv535)
53. Wang D, Treado JD, Boromand A, Norwick B, Murrell MP, Shattuck MD, O'Hern CS. 2021 The structural, vibrational, and mechanical properties of jammed packings of deformable particles in three dimensions. *Soft Matter* **17**, 9901–9915. (doi:10.1039/D1SM01228B)
54. Zhang L, Ambrose C. 2022 CLASP balances two competing cell division plane cues during leaf development. *Nat. Plants* **8**, 682–693. (doi:10.1038/s41477-022-01163-5)
55. Schindelin J *et al.* 2012 Fiji: an open-source platform for biological-image analysis. *Nat. Methods* **9**, 676–682. (doi:10.1038/nmeth.2019)
56. Wan Y, Otsuna H, Chien CB, Hansen C. 2012 FluoRender: an application of 2D image space methods for 3D and 4D confocal microscopy data visualization in neurobiology research. In *2012 IEEE Pacific Visualization Symp., Songdo, South Korea, 28 February–2 March*, pp. 201–208.
57. Paganin D, Mayo SC, Gureyev TE, Miller PR, Wilkins SW. 2002 Simultaneous phase and amplitude extraction from a single defocused image of a homogeneous object. *J. Microsc.* **206**, 33–40. (doi:10.1046/j.1365-2818.2002.01010.x)
58. Théroux-Rancourt G, Earles JM, Gilbert ME, Zwieniecki MA, Boyce CK, McElrone AJ, Brodersen CR. 2017 The bias of a two-dimensional view: comparing two-dimensional and three-dimensional mesophyll surface area estimates using noninvasive imaging. *N. Phytol.* **215**, 1609–1622. (doi:10.1111/nph.14687)
59. Vincent L, Soille P. 1991 Watersheds in digital spaces: an efficient algorithm based on immersion simulations. *IEEE Trans. Pattern Anal. Mach. Intell.* **13**, 583–598. (doi:10.1109/34.87344)
60. Treado JD, Roddy AB, Théroux-Rancourt G, Zhang L, Ambrose C, Brodersen CR, Shattuck MD, O'Hern CS. 2022 Localized growth and remodelling drives spongy mesophyll morphogenesis. OSF. (doi:10.17605/OSF.IO/C4RBM)
61. Treado JD, Roddy AB, Théroux-Rancourt G, Zhang L, Ambrose C, Brodersen CR, Shattuck MD, O'Hern CS. 2022 Localized growth and remodelling drives spongy mesophyll morphogenesis. Figshare. (doi:10.6084/m9.figshare.c.6307516)